Journal of Quantitative Spectroscopy & Radiative Transfer 132 (2014) 3–11

Contents lists available at ScienceDirect

Journal of Quantitative Spectroscopy & Radiative Transfer

journal homepage: www.elsevier.com/locate/jqsrt

Review

Fluctuational electrodynamics calculations of near-field heat transfer in non-planar geometries: A brief overview

Clayton R. Otey [a], Linxiao Zhu [a], Sunil Sandhu [b], Shanhui Fan [b,*]

[a] Department of Applied Physics, Stanford University, Stanford, CA 94305, USA
[b] Department of Electrical Engineering, Stanford University, Stanford, CA 94305, USA

ARTICLE INFO

Article history:
Received 20 September 2012
Received in revised form
13 March 2013
Accepted 16 April 2013
Available online 3 May 2013

Keywords:
Near field
Radiative
Heat transfer
Computational
Scattering
Boundary element
FDTD

ABSTRACT

Near-field electromagnetic heat transfer is of interest for a variety of applications, including energy conversion, and precision heating, cooling and imaging of nanostructures. This past decade has seen considerable progress in the study of near-field electromagnetic heat transfer, but it is only very recently that numerically exact methods have been developed for treating near-field heat transfer in the fluctuational electrodynamics formalism for non-trivial geometries. In this paper we provide a tutorial review of these exact methods, with an emphasis on the computational aspects of three important methods, which we compare in the context of a canonical example, the coupled dielectric sphere problem.

Contents

1. Introduction

Heat will flow between bodies at different temperatures. Among the mechanisms of heat transfer, radiative electromagnetic heat transfer is special in that it may

* Corresponding author.
E-mail addresses: otey@stanford.edu, clayton.otey@gmail.com (C.R. Otey), linxiao@stanford.edu (L. Zhu), shanhui@stanford.edu (S. Fan).

0022-4073/$ - see front matter © 2013 Elsevier Ltd. All rights reserved.
http://dx.doi.org/10.1016/j.jqsrt.2013.04.017

transmit heat through vacuum. When certain classes of dielectric bodies are in close proximity, so that their separation falls below the characteristic thermal wavelength $\lambda_T = hc/k_B T$, we observe the near-field regime, where the heat flow can be enhanced beyond the constraint of the Planck law that governs far-field heat transfer. Such an enhancement has been demonstrated in a number of recent experiments [1–4], leading to the prospect of applying near-field heat transfer in areas including non-contact radiative cooling [5], thermal imaging [6,7], thermal circuit elements [8–11], as well as energy conversion and thermo-photo-voltaics [12–16].

These experimental developments have in turn motivated theoretical studies of the mathematical and computational underpinnings of near-field heat transfer. What has emerged is a clear need for exact methods to calculate electromagnetic heat transfer in the fluctuational electrodynamics formalism [17]. It is important to state up front that the quantum electrodynamics formalism yields the same results, provided the thermodynamic interpretation is appropriate; in particular it must be assumed that the sources are in local equilibrium with a thermal reservoir [18].

Using the fluctuational electrodynamics formalism, we can calculate heat flux between two bodies separated by a vacuum gap, as shown in Fig. 1a. The problem is completely specified by the temperature distribution $T(\mathbf{r})$ and relative dielectric function of the materials, $\epsilon(\mathbf{r},\omega) = \epsilon'(\mathbf{r},\omega) + i\epsilon''(\mathbf{r},\omega)$. We work with the time-harmonic form of Maxwell's equations, with implicit $\propto e^{-i\omega t}$ time-dependent factors, so a positive imaginary part of the dielectric functions, $\epsilon''(\mathbf{r},\omega)$, corresponds to material loss. We limit our discussion to the case of homogenous dielectric bodies, so that $\epsilon(\mathbf{r},\omega) = \epsilon_n(\omega)$ in the various regions $n \in 0,1,2$. Free space corresponds to $n=0$, and is spatially unbounded, with $\epsilon_0 = \lim_{\delta\to 0} 1 + \delta i$. The dielectric constants are typically assumed to be local, i.e. depends on the frequency but not the wave vector of the excitation. One expects that such a local dielectric function should be applicable unless one is in the deep near-field regime where the size of the vacuum gap is reduced to a few nanometers [7,19]. We note that in this regime, other mechanisms of heat transfer may come into play, such as phonon transport [20], but we do not consider these mechanisms in this review. Regarding the temperature distribution, we assume that the temperature is uniform in each region; we label these temperatures T_n.

The sources of electromagnetic heat transfer are thermally fluctuating current density distributions $J_i(\mathbf{r},\omega)$ within the bodies; see Fig. 1b. For the purpose of calculating ensemble-averaged heat transfer in a stationary system, it suffices to know the two-point spectral correlation function of the current densities, which for a system in local thermal equilibrium is given by the fluctuation–dissipation theorem [21–23]. We use the time-harmonic form of the theorem, and thus we already assume a stationary process. Here and throughout, an overbar will denote an ensemble average. The theorem holds in general for dissipative linear systems. In the present case, the dissipation is due to dielectric losses, and we write

$$\overline{J_i(\mathbf{r},\omega)J_k^*(\mathbf{r}',\omega)} = \frac{4}{\pi}\omega\Theta(\omega,T)\delta(\mathbf{r}-\mathbf{r}')\mathrm{Im}[\epsilon(\mathbf{r},\omega)]\epsilon_0\delta_{ik} \tag{1}$$

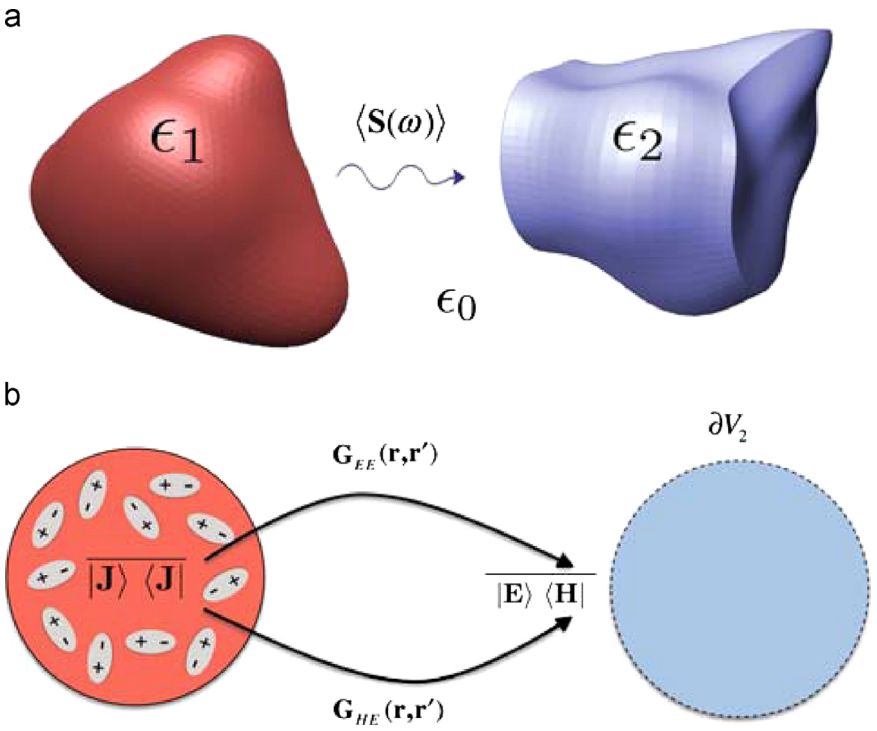

Fig. 1. (a) Near-field heat transfer between two non-planar bodies V_1 and V_2 with dielectric functions ϵ_1 and ϵ_2, separated by vacuum and maintained at temperatures T_1 and T_2, respectively. (b) Schematic of a fluctuational electrodynamics calculation in the Green function picture. The current–current correlations in V_1 are specified by the fluctuation–dissipation theorem, and are related via the dyadic Green functions $\mathbf{G}_{EE}$ and $\mathbf{G}_{HE}$ to the field–field correlations, and thus the ensemble-averaged Poynting vector on the boundary of V_2.

where the mean spectral thermal energy is given by $\Theta(\omega,T)=\hbar\omega/(\exp(\hbar\omega/k_BT)-1)$, and i and k label different spatial directions. With the sources specified, the **E** and **H** fields can be expressed in terms of dyadic Green functions (also referred to as Green dyads) for the time-harmonic Maxwell's equations,

$$\mathbf{E}(\mathbf{r},\omega)=i\omega\mu_0\int \mathbf{G}_{EE}(\mathbf{r},\mathbf{r}',\omega)\cdot\mathbf{J}(\mathbf{r}',\omega) \tag{2}$$

$$\mathbf{H}(\mathbf{r},\omega)=\int \mathbf{G}_{HE}(\mathbf{r},\mathbf{r}',\omega)\cdot\mathbf{J}(\mathbf{r}',\omega) \tag{3}$$

We will make use of the concise operator notation whenever possible [24]. A brief review on this notation can be found in Appendix A. For example, Eqs. (1)–(3) above become

$$\overline{|\mathbf{J}\rangle\langle\mathbf{J}|}=\frac{4}{\pi}\omega\Theta\,\mathrm{Im}[\epsilon]\epsilon_0\mathbb{I} \tag{4}$$

$$|\mathbf{E}\rangle=i\omega\mu_0\mathbb{G}_{EE}|\mathbf{J}\rangle \tag{5}$$

$$|\mathbf{H}\rangle=\mathbb{G}_{HE}|\mathbf{J}\rangle \tag{6}$$

In Eq. (4), $\mathbb{I}$ is the identity operator over all indices, including a delta $\int d\mathbf{r}\,\delta^3(\mathbf{r}-\mathbf{r}')\bullet$ term. In general, ϵ is a tensor, and the operator notation is indifferent to the form of this tensor. In our computational examples, though, we will assume an isotropic dielectric, which is adequate for describing most metal and dielectric systems.

The spectral energy flux into V_2 due to sources in V_1 can be calculated by integrating the associated time-harmonic Poynting vector over the surface ∂V_2

$$S(\omega)=\frac{1}{2}\,\mathrm{Re}\int_{\partial V_2} d\hat{\mathbf{n}}\cdot\overline{\mathbf{E}(\mathbf{r},\omega)\times\mathbf{H}^*(\mathbf{r},\omega)} \tag{7}$$

Here, $\hat{\mathbf{n}}$ is the outward pointing normal. The correlation of the **E** and **H** fields, due to sources inside V_1, follows from Eqs. (1)–(3) as

$$\begin{aligned}\overline{|\mathbf{E}\rangle\langle\mathbf{H}|}&=i\omega\mu_0\mathbb{G}_{EE}\overline{|\mathbf{J}\rangle\langle\mathbf{J}|}\mathbb{G}_{HE}^{\dagger}\\&=i\frac{4}{\pi}(\omega/c)^2\Theta(\omega,T_1)\mathrm{Im}[\epsilon_1]\mathbb{G}_{EE}\mathbb{G}_{HE}^{\dagger}\end{aligned} \tag{8}$$

The total heat flux is just the integral of the spectral heat flux in Eq. (7), $S=\int_0^\infty d\omega\,S(\omega)$. Fig. 1b displays a schematic of this formalism.

One can reformulate Eq. (8) as a double volume integral, which can be absorbed into a trace in the operator formalism. Following Krüger et al. [24, Section III.B], we may write this as

$$S(\omega)=\frac{2}{\pi}\,\mathrm{Im}\,\mathrm{Tr}[\overline{|\mathbf{E}\rangle\langle(\omega\mu_0\mathbb{G}_{EE}^0)^{-1}\mathbf{E}|}] \tag{9}$$

where $\mathbb{G}_{EE}^0$ is the homogenous, free-space electric field Green dyad.

Of course, heat flows from V_2 to V_1, as well, and the physically measurable quantity is the *net* heat transfer. Fortunately, reciprocity of the Green functions manifests a necessary consequence of detailed balance: at equilibrium the net heat transfer must vanish, and so when $T_1=T_2$, the heat flux into V_2 due to sources in V_1 must equal the heat flux into V_1 due to sources in V_2. From a computational standpoint, then, we may therefore limit our attention to sources in V_1, effectively treating V_2 as a zero temperature body. To recover the net heat flux when $T_2\neq0$, we simply replace $\Theta(\omega,T_1)$ by $\Theta(\omega,T_1)-\Theta(\omega,T_2)$.

A direct implementation of the fluctuational electrodynamic treatment of near-field electromagnetic heat transfer typically involves integration over a large number of sources and frequencies, which for arbitrary geometries can be very computationally demanding. While the basic formalism was developed in the 1950s [17], for several decades afterwards exact calculations of near-field electromagnetic heat transfer were restricted to planar geometries [25,26]. The theory for planar surfaces has been subsequently extended to treat, for example, structures with surface roughness [27] and nano-porous materials [28].

For non-planar geometries, a number of approximate methods have been developed [2,29–32]. The dipole approximation was developed to treat the heat transfer between a deep sub-wavelength nano-particle and a planar substrate [29,31]. The proximity approximation, which was also extensively applied, approximates the two bodies in terms of a series of parallel planes [2]. One should note however that the proximity approximation is an uncontrolled approximation in the sense that there is no systematic process through which one can improve the approximation towards an exact result. Also, the proximity approximation does not reproduce the correct far-field results when the two bodies are far apart from each other [32].

One of the most significant recent developments in the past few years is the developments of exact numerical calculations of near-field heat transfer between dielectrics in non-planar geometries. In this paper, we provide a brief tutorial review of such developments, with an emphasis on the computational aspects involved. We begin with the partial-wave scattering matrix approach in Section 2, which is well suited for treating highly symmetric geometries such as coupled-sphere and sphere-plate. In Section 3, we discuss the use of the boundary element method (BEM). In Section 4, we discuss the finite-difference time-domain method, for treating arbitrary geometries in a statistical manner. Finally, in Section 5, we compare all these methods with an illustrative example, where we solve a coupled-sphere problem with all three different methods.

2. Partial-wave scattering method

2.1. Green function picture

The coupled microsphere geometry was the first non-planar geometry treated exactly with the fluctuational electrodynamics formalism. The approach of Narayanaswamy and Chen in [33] was to calculate the Green dyad's in Eq. (8) directly, by matching boundary conditions in a vector spherical harmonic partial-wave expansion, and perform the source volume and flux surface integration using orthonormality properties of this basis. For concreteness, our discussion below will often make reference to this original coupled-sphere problem. We will use a more general notation, though, closely following the work of Krüger et al. [34; 35, Section IV; 24, Section VII]. We aim to

emphasize how this intuitive Green function picture can be related to an elegant field-correlator picture, which actually makes no reference to the sources.

To set notation, we work below with a basis of vector wave function solutions $\{|\mathbf{\Phi}_\alpha\rangle\}$ to the Maxwell equation,

$$\nabla\times\nabla\times|\mathbf{\Phi}_\alpha\rangle-(\omega/c)^2|\mathbf{\Phi}_\alpha\rangle=0 \tag{10}$$

These basis functions span a Hilbert space, with the usual inner product [36]. Here, and throughout the paper, we sum over repeated indices unless otherwise noted in the text. A key property of these functions is that they have a well-defined and coordinate-free relationship to the free-space Green dyads, e.g.

$$\mathbb{G}^0_{EE}=i(\omega/c)|\mathbf{\Phi}^{'\mathrm{out}}_\alpha\rangle\langle\mathbf{\Phi}^{'\mathrm{reg}}_\alpha| \tag{11}$$

Referring now to the coupled-sphere example, we use a vector spherical harmonic basis, and $\alpha\in\{l,m,P\}$ labels the degree l, order m, and polarization P (M wave or N wave) of the orthonormal basis of spherical harmonics, and $|\mathbf{\Phi}'_{l,m,P}\rangle=|\mathbf{\Phi}_{l,-m,P}\rangle$.

$\mathbb{G}^0_{HE}$ can be decomposed in a similar manner, with the polarization for the $\mathbf{r}$ partial wave swapped (M waves become N waves and vice versa), which we denote with the replacement $|\mathbf{\Phi}\rangle\to|\tilde{\mathbf{\Phi}}\rangle$

$$\mathbb{G}^0_{HE}=i(\omega/c)^2|\tilde{\mathbf{\Phi}}^{'\mathrm{out}}_\alpha\rangle\langle\mathbf{\Phi}^{'\mathrm{reg}}_\alpha| \tag{12}$$

The inhomogenous Green functions can be obtained by applying a scattering operator $\mathbb{O}$ to the free-space Green function $\mathbb{G}^0_{EE}$, which acts on the outgoing partial-wave only, i.e.

$$\mathbb{G}_{EE}=\mathbb{O}\mathbb{G}^0_{EE} \tag{13}$$

$$\mathbb{G}_{EE}=i(\omega/c)O_{\alpha\beta}|\mathbf{\Phi}^{'\mathrm{out}}_\beta\rangle\langle\mathbf{\Phi}^{'\mathrm{reg}}_\alpha| \tag{14}$$

$\mathbb{O}$ is defined to act on a partial-wave solution of the Maxwell equations in homogenous space (the incident field), and return the total field when V_1 and V_2 are present [37,24].

If we restore the position dependence of the fields and dyads, we may write the field correlations, due to sources inside V_1, as

$$\begin{aligned}\overline{\langle\mathbf{r}|\mathbf{E}\rangle\langle\mathbf{H}|\mathbf{r}'\rangle}_{\mathrm{body}}=&\frac{4}{\pi}(\omega/c)^2\Theta(\omega,T_1)\\&\times\left(\int_{V_1}d\mathbf{r}''\,\epsilon''_1(\omega/c)^3\langle\mathbf{r}''|\mathbf{\Phi}^{'\mathrm{reg}}_\alpha\rangle\langle\mathbf{\Phi}^{'\mathrm{reg}}_\beta|\mathbf{r}''\rangle\right)\\&\times O_{\alpha\gamma}\langle\mathbf{r}|\mathbf{\Phi}^{'\mathrm{out}}_\gamma\rangle\langle\tilde{\mathbf{\Phi}}^{'\mathrm{out}}_\rho|\mathbf{r}'\rangle O^\dagger_{\beta\rho}\end{aligned} \tag{15}$$

Note that the volume integral over sources is now independent of the scattering, and can be performed analytically using orthonormality of $\{|\mathbf{\Phi}_\alpha\rangle\}$. The remainder of the computation is thus reduced to determining the scattering operator $O_{\alpha\beta}$. It suffices to know the $\mathbb{T}$ operators $\mathbb{T}_1$ and $\mathbb{T}_2$ for the isolated bodies in a suitable basis, and the translation operators $\mathbb{U}_{12}$ and $\mathbb{U}_{21}$, which express the linear relationship between the partial-waves sourced by body 1 and body 2, in their respective bases. The $\mathbb{T}$ matrices for the individual bodies, which contain the reflection coefficients for the partial waves in the basis for that body, are defined to satisfy

$$|\mathbf{\Phi}^{'\mathrm{tot}}_\alpha\rangle=|\mathbf{\Phi}^{'\mathrm{reg}}_\alpha\rangle+\mathbf{T}_{\alpha\beta}|\mathbf{\Phi}^{'\mathrm{out}}_\beta\rangle \tag{16}$$

where $|\mathbf{\Phi}^{'\mathrm{tot}}_\alpha\rangle$ represents the total field resulting from scattering the homogenous free space solutions $|\mathbf{\Phi}^{'\mathrm{reg}}_\alpha\rangle$ in the presence of the body.

In the coupled-sphere problem, the $\mathbb{U}$ operators are matrices with elements given by the vector translation addition theorem which expresses vector spherical harmonics centered at V_1 in terms of a similar basis with origin at the center of V_2. We arrive at a linear system for $\mathbb{O}$ by expressing waves sourced from V_1 and V_2 in a single basis using the $\mathbf{T}$ and $\mathbf{U}$ matrices,

$$\mathbf{O}=(\mathbf{I}-\mathbf{T}_1\mathbf{U}_{12}\mathbf{T}_2\mathbf{U}_{21})^{-1} \tag{17}$$

In the coupled-sphere problem, we truncate the α basis to $\{1\ldots l_{max},-m_{max}\ldots m_{max}\}$. Because of azimuthal symmetry in this case, we find that $\mathbf{O}$ splits into blocks, indexed by m. Each m contribution involves a linear solve for $2l_{max}$ unknown partial wave coefficients.

Eq. (15) expresses the field correlations in the partial-wave basis for body 1. In order to obtain the partial-wave coefficients in the basis for body 2, we multiply by $(\mathbf{I}+\mathbf{T}_2\mathbf{U}_{21})$. Then we may easily perform the surface integral of the Poynting flux over ∂V_2 using orthonormality of the body 2 basis. A similar procedure can be used in the sphere-plate geometry [34,38,39], and in principle for other systems where orthonormality of the bases can be used to analytically perform the spatial integrals.

2.2. Field correlator picture

Alternatively, one can avoid explicit reference to the current–current correlation function and the Green dyads, in favor of field–field correlators. In Section III.A of [24], Krüger et al. derive an expression for the radiation from a body in terms of the single body $\mathbf{T}$-matrix. This in turn allows them to write the heat transfer as the trace of a matrix, which is constructed entirely from scattering $\mathbf{T}$ and translation $\mathbf{U}$ matrices. Here we briefly outline the idea, closely following their original arguments, but with a slightly different notation.

The starting point is the fluctuation–dissipation theorem for the electric field correlator in the absence of the body [35,24]. In thermal equilibrium the bodies are at the same temperature and there is no net heat flux, and the fluctuation–dissipation theorem applied to the electric-field fluctuations yields

$$\begin{aligned}\overline{|\mathbf{E}\rangle\langle\mathbf{E}|}_{\mathrm{eq}}&=\mu_0\omega(4/\pi)\Theta(\omega,T)\mathrm{Im}[\mathbb{G}_{EE}]\\&=a(\omega,T)\mathrm{Re}[|\mathbf{\Phi}^{\mathrm{reg}}_\alpha+\mathbf{T}_{\alpha\beta}\mathbf{\Phi}^{\mathrm{out}}_\beta\rangle\langle\mathbf{\Phi}^{'\mathrm{reg}}_\alpha|]\\&=a(\omega,T)|\mathbf{\Phi}^{\mathrm{reg}}_\alpha+\mathbf{T}_{\alpha\beta}\mathbf{\Phi}^{\mathrm{reg}}_\beta\rangle\langle\mathbf{\Phi}^{'\mathrm{reg}}_\alpha|\end{aligned} \tag{18}$$

where $a(\omega,T)=\frac{4\omega^2}{\pi\epsilon_0c^3}\Theta(\omega,T)$.

One can decompose the field correlator in Eq. (18):

$$\overline{|\mathbf{E}\rangle\langle\mathbf{E}|}_{\mathrm{eq}}=\overline{|\mathbf{E}\rangle\langle\mathbf{E}|}_{\mathrm{body}}+\overline{|\mathbf{E}\rangle\langle\mathbf{E}|}_{\mathrm{env}} \tag{19}$$

The environmental correlator is sourced by the free-space region V_0 [22,24,35,30], and can be expressed by

applying T-matrices to the partial-wave expansion of $\mathbb{G}^0_{EE}$,

$$\overline{|\mathbf{E}\rangle\langle\mathbf{E}|}_{\text{env}} = a(\omega,T)|\boldsymbol{\Phi}^{'\text{reg}}_\alpha + \mathbf{T}_{\alpha\beta}\boldsymbol{\Phi}^{'\text{out}}_\beta\rangle\langle\boldsymbol{\Phi}^{'\text{reg}}_\alpha + \mathbf{T}_{\alpha\beta}\boldsymbol{\Phi}^{'\text{out}}_\beta| \quad (20)$$

The correlator due to sources integrated inside the body then follows from Eq. (19),

$$\overline{|\mathbf{E}\rangle\langle\mathbf{E}|}_{\text{body}} = a(\omega,T)\mathbb{R}_{\alpha\beta}|\boldsymbol{\Phi}^{'\text{out}}_\alpha\rangle\langle\boldsymbol{\Phi}^{'\text{out}*}_\beta| \quad (21)$$

where the $\mathbf{R}$ matrix contains all of the information about emission, and is defined in terms of the $\mathbf{T}-$matrix, as

$$\mathbf{R} = -\tfrac{1}{2}(\mathbf{T}+\mathbf{T}^\dagger) - \mathbf{T}\mathbf{T}^\dagger \quad (22)$$

The presence of the 2nd body can be accounted for by applying the $O_{\alpha\beta}$ scattering operator from Eq. (17) to each field in the tensor product in Eq. (21). This gives the inhomogenous field correlation, and as a result, a trace formula for $S(\omega)$ may be written as

$$S(\omega) = \theta(\omega,T)^2\frac{2}{\pi}\,\text{Tr}\{\mathbf{R}_2^*\mathbf{W}\mathbf{R}_1\mathbf{W}^\dagger\} \quad (23)$$

where $\mathbf{W} = (\mathbf{I}-\mathbf{U}_{21}\mathbf{T}_1\mathbf{U}_{12}\mathbf{T}_2)^{-1}\mathbf{U}_{21}$.

From a computational perspective, the calculation of the $\mathbf{W}-$matrix is essentially the same as the calculation of $\mathbf{O}$, described in the previous section. One needs to determine the reflection coefficients and translation operators for the system and solve a linear system with a truncated basis. However, the theoretical framework here is considerably more elegant, and can be generalized to any coordinate system (see [24, Section VII]). Furthermore, for arbitrary geometries, one could calculate elements of the $\mathbf{T}$-matrices for each body separately using any numerical method at one's disposal, and then use these same trace formulae [37]. Of course, the coordinate systems for each body must be appropriate for the geometry. If there exists a plane that does not intersect either of the bodies, then a plane wave basis will work [40]; if a body can be enclosed by sphere which does not intersect the other bodies, then a spherical basis is appropriate for that body's $\mathbf{T}-$matrix.

3. Boundary element method

With the boundary element we consider, instead of partial-wave solutions to the homogenous Maxwell's equations, the scattered fields which are sourced by the tangential $\mathbf{E}$ and $\mathbf{H}$ fields on the *boundaries* of the bodies, considered as equivalent current sources. Given any incident field configuration, these tangential surface fields are uniquely determined, and they completely specify the scattered fields.

More specifically, we introduce $\{|\mathbf{f}_\alpha\rangle\}$, a set of orthonormal vector-valued functions with support on $\partial V_{1,2}$. We then expand the surface currents

$$\begin{pmatrix}|\hat{\mathbf{n}}\times\mathbf{H}\rangle\\ |\mathbf{E}\times\hat{\mathbf{n}}\rangle\end{pmatrix} = \eta_\alpha|\mathbf{f}_\alpha\rangle \quad (24)$$

and the tangential fields

$$\begin{pmatrix}|\mathbf{E}_t\rangle\\ |\mathbf{H}_t\rangle\end{pmatrix} = \phi_\alpha|\mathbf{f}_\alpha\rangle \quad (25)$$

The coefficients for the surface currents η_α and the tangential fields ϕ_α become the objects of interest in the well known boundary element method (BEM) [41–43]. The BEM provides an efficient means of relating incident and scattered fields on $\partial V_{1,2}$.

Using the BEM formalism, we can approach the near-field heat transfer problem from two pictures, very much the same as in the previous section. The first is a direct approach based on the Green function picture, i.e. calculating the Green dyads in Eq. (8) explicitly, and integrating over all source configurations. The second approach involves constructing the non-equilibrium, inhomogenous field correlators from the equilibrium, homogenous Green functions and scattering operators.

3.1. Green function picture

In the Green function picture, we consider a set of volumetric current density distributions $\mathbf{J}^i$ with support inside V_1, as in Fig. 1 and solve for the fields $\mathbf{E}^i$ and $\mathbf{H}^i$ on ∂V_2 (See again Fig. 1b). The superscript i indexes this set of current sources. We follow the notation of Reid et al. [42–44], and carry over some content from Chew [45].

For each $\mathbf{J}^i$, the boundary element method gives a linear system

$$M_{\alpha\beta}\eta^i_\beta = \phi^i_\alpha \quad (26)$$

where

$$\mathbf{M} = \begin{pmatrix}\mathbf{Z}^{\epsilon_1}_{11}+\mathbf{Z}^{\epsilon_0}_{11} & \mathbf{Z}^{\epsilon_0}_{12}\\ \mathbf{Z}^{\epsilon_0}_{21} & \mathbf{Z}^{\epsilon_2}_{22}+\mathbf{Z}^{\epsilon_0}_{22}\end{pmatrix} \quad (27)$$

The $\mathbf{Z}^\epsilon$ blocks contain interactions between the basis functions via the Green dyads $\mathbb{G}^\epsilon_{EE}$ and $\mathbb{G}^\epsilon_{EH}$ for a homogenous space with dielectric constant ϵ,

$$(Z^\epsilon_{mn})_{\alpha\beta} = \left\langle \mathbf{f}_\alpha \middle| \begin{matrix} i\omega\mu_0\mathbb{G}^\epsilon_{EE} & \mathbb{G}^\epsilon_{EH}\\ -\mathbb{G}^\epsilon_{EH} & i\omega\epsilon\epsilon_0\mathbb{G}^\epsilon_{EE}\end{matrix} \middle| \mathbf{f}_\beta \right\rangle, \quad \begin{matrix}\mathbf{r}\in\partial V_m\\ \mathbf{r}'\in\partial V_n\end{matrix}. \quad (28)$$

The solution of Eq. (26) is sufficient for determining $S^i(\omega)$ as

$$\begin{aligned} S^i(\omega) &= \frac{1}{2}\int_{\partial V_2} d\hat{\mathbf{n}}\cdot\overline{\mathbf{E}^i\times\mathbf{H}^{i*}}\\ &= \frac{1}{4}\int_{\partial V_2} dS\overline{\begin{pmatrix}\mathbf{E}\\ \mathbf{H}\end{pmatrix}\cdot\begin{pmatrix}\hat{\mathbf{n}}\times\mathbf{H}^*\\ \mathbf{E}^*\times\hat{\mathbf{n}}\end{pmatrix}}\\ &= \frac{1}{4}\,\text{Tr}\{(\mathbf{Z}_2\boldsymbol{\eta}^{2,i})(\boldsymbol{\eta}^{2,i})^\dagger\} \end{aligned} \quad (29)$$

In the last line, $\eta^{2,i}$ are those components of η that lie on the surface of body 2, and we have used the relation $\phi^{2,i}_\alpha = (Z_2)_{\alpha\beta}\eta^{2,i}_\beta$. The integral is approximated as a trace over all basis functions with support on ∂V_2.

With the BEM described above, we can calculate the matrix $\mathbf{M}$ once per frequency, invert it, and use it to calculate $S(\omega)\propto\sum_i S^i(\omega)$ for a complete set of $\boldsymbol{\phi}^{\mathbf{i}}$ associated with dipole sources distributed uniformly throughout V_1.

3.2. Field correlator picture

There is an interesting connection between the BEM formalism and the field correlator picture discussed in Section 2.2 which gives a direct route to a trace formula

similar to Eq. (23),

$$S(\omega) = \theta(\omega, T)\frac{2}{\pi}\mathrm{Tr}\,\mathbf{Q}_2\mathbf{M}^{-1}\mathbf{Q}_1(\mathbf{M}^{-1})^\dagger \tag{30}$$

where

$$\mathbf{Q}_1 = \frac{1}{2}\begin{pmatrix} \mathbf{Z}_{11}^{\epsilon_1} + (\mathbf{Z}_{11}^{\epsilon_1})^\dagger & 0 \\ 0 & 0 \end{pmatrix} \tag{31}$$

$$\mathbf{Q}_2 = \frac{1}{2}\begin{pmatrix} 0 & 0 \\ 0 & \mathbf{Z}_{22}^{\epsilon_2} + (\mathbf{Z}_{22}^{\epsilon_2})^\dagger \end{pmatrix} \tag{32}$$

The **M** and **Z** matrices are precisely those defined in Eqs. (27) and (28).

This formula was first derived in [44] without reference to the correlator picture. But the form of Eq. (30) suggests a connection to the trace formula (23) derived in Section 2. In fact, one can construct Eq. (30) as follows.

First consider a homogenous space with $\epsilon(\mathbf{r}) = \epsilon_1$. Note that this is the material that composes the first body, not vacuum. The equilibrium field correlations can be written in matrix form, as in the vacuum case,

$$\begin{aligned}\left(\overline{\phi_\alpha \phi_\beta^*}\right)_{\mathrm{eq}} &= \left\langle \mathrm{f}_\alpha \left| \begin{matrix} \overline{|\mathbf{E}\rangle\langle\mathbf{E}|} & \overline{|\mathbf{E}\rangle\langle\mathbf{H}|} \\ \overline{|\mathbf{H}\rangle\langle\mathbf{E}|} & \overline{|\mathbf{H}\rangle\langle\mathbf{H}|} \end{matrix} \right| \mathrm{f}_\beta \right\rangle_{eq} \\ &= \theta(\omega, T)\left\langle \mathrm{f}_\alpha \left| \begin{matrix} \omega\mu_0\,\mathrm{Im}[\mathbf{G}_{EE}^{\epsilon_1}] & i\,\mathrm{Im}[\mathbf{G}_{HE}^{\epsilon_1}] \\ i\,\mathrm{Im}[\mathbf{G}_{EH}^{\epsilon_1}] & \omega\epsilon_1\,\mathrm{Im}[\mathbf{G}_{E}^{\epsilon_1}] \end{matrix} \right| \mathrm{f}_\beta \right\rangle \\ &= \theta(\omega, T)\frac{1}{2}\left(\mathbf{Z}_{11}^{\epsilon_1} + (\mathbf{Z}_{11}^{\epsilon_1})^\dagger\right)\alpha_\beta \end{aligned} \tag{33}$$

Here we have used the definition of the **Z** matrices in Eq. (28), and reciprocity of the Green dyads. The equilibrium field correlations in Eq. (33) contain contributions from both the body and from the environment.

We now turn our attention to the correlation of the surface currents due to sources in body 1. Eq. (26) provides the necessary connection between the homogenous (incident) fields and inhomogenous (incident plus scattered) fields. The key step is to restrict the incident fields to body 1, so that the environmental contribution to the equilibrium correlation is not included when solving for the inhomogenous surface currents. This gives a modified BEM equation,

$$\mathbf{M}\begin{pmatrix} \boldsymbol{\eta}^1 \\ \boldsymbol{\eta}^2 \end{pmatrix} = \begin{pmatrix} \mathbf{I} & 0 \\ 0 & 0 \end{pmatrix}\begin{pmatrix} \boldsymbol{\phi}^1 \\ \boldsymbol{\phi}^2 \end{pmatrix} \tag{34}$$

From Eqs. (33) and (34), we can derive the correlation of the surface current coefficients,

$$\begin{aligned}\overline{\boldsymbol{\eta}\boldsymbol{\eta}^*} &= \mathbf{M}^{-1}\begin{pmatrix} \mathbf{I} & 0 \\ 0 & 0 \end{pmatrix}\overline{\boldsymbol{\phi}\boldsymbol{\phi}^*}_{\mathrm{eq}}\begin{pmatrix} \mathbf{I} & 0 \\ 0 & 0 \end{pmatrix}(\mathbf{M}^{-1})^\dagger \\ &= \theta(\omega, T)\mathbf{M}^{-1}\mathbf{Q}_1(\mathbf{M}^{-1})^\dagger \end{aligned} \tag{35}$$

We finally arrive at Eq. (30) by appalying to the left of Eq.(35), which isolates the scattered fields on αV_2, as in Eq. (29). The BEM trace formula (30) has the same form as the **T**−matrix formula in Eq. (23). However, the BEM formula is not merely a special case of the **T**−matrix formula. The **Q** matrices are associated with the equilibrium, homogenous fields in V_1, whereas the **R** operators in Eq. (23) are associated with the single body radiation fields.

The BEM formalism can also be used to calculate **T**−matrix elements for bodies which do not have the same symmetry as the partial-wave coordinate systems. This may be accomplished by solving the BEM problem in Eq. (26) $M_{\gamma\beta}\eta_\beta^\alpha = \langle \mathbf{f}_\gamma | \Phi_\alpha \rangle$ for each partial-wave Φ_α in the truncated basis associated with the coordinate system. Then $\mathbf{T}_n$ can be expressed as $\mathbf{T}_n = Z_{nn}^{\epsilon_n}\eta^\alpha$. This type of procedure was first used by McCauley et al. for calculating heat transfer between a probe and a plane [37], using a cylindrical plane-wave basis.

4. Finite difference time domain method

In this section we describe how the finite-difference time-domain (FDTD) method [46] can be used to calculate heat transfer by incorporating the Langevin approach to Brownian motion [47–49]. In this approach, we model the polarization response $\mathbf{P}(t)$ of a system to a local electric field $\mathbf{E}(t)$ and a random force term $\mathbf{K}(t)$ using the following equation of motion:

$$\frac{d^2\mathbf{P}}{dt^2} + \gamma\frac{d\mathbf{P}}{dt} + \omega_0^2\mathbf{P} = \sigma\mathbf{E} + \mathbf{K} \tag{36}$$

where γ is the frictional coefficient of the polarization system, ω_0 is its resonance frequency and σ is its strength. The random force term $\mathbf{K}(t)$ is a fluctuating source that gives rise to thermal radiation.

After discretizing Eq. (36) and specifying $\mathbf{K}(t)$, we can perform time-stepping updates of $\mathbf{P}(t)$ and $\mathbf{E}(t)$ using the conventional FDTD algorithm [47]. From this numerical simulation of thermal emission, we can calculate the heat flux spectrum in an arbitrarily shaped geometry.

We first describe how the random force term $\mathbf{K}(t)$ can be specified in order to model the thermal fluctuations in the electromagnetic field. The polarization component of the displacement field $\mathbf{D} = \epsilon_0\mathbf{E} + \mathbf{P}$ contains a random component with spectral amplitude [48]

$$\mathbf{Q}(\mathbf{r}, \omega) = \frac{\mathbf{K}(\mathbf{r}, \omega)}{\omega_0^2 - \omega^2 - i\gamma\omega} \tag{37}$$

$\mathbf{Q}(r, \omega)$ is related to the current $\mathbf{J}(\mathbf{r}, \omega) = -i\omega\mathbf{Q}(\mathbf{r}, \omega)$ and

$$\epsilon''(\omega) = \mathrm{Im}\left[\epsilon_0 + \frac{|\mathbf{P}|}{|\mathbf{E}|}\right] = \frac{\sigma\gamma\omega}{(\omega_0^2 - \omega^2)^2 + \gamma^2\omega^2}.$$

By combining the fluctuation–dissipation theorem for the currents in Eq. (1) with Eq. (37), we find the correlation function for $\mathbf{K}(\mathbf{r}, \omega)$ [48],

$$\overline{K_\alpha(\mathbf{r}, \omega)K_\beta^*(\mathbf{r}', \omega)} = \frac{4}{\pi}\sigma\gamma\Theta(\omega, T)\delta_{\alpha\beta}\delta(\mathbf{r} - \mathbf{r}'). \tag{38}$$

This expression for the **K** correlation function gives us information about the distribution of the random force term. For FDTD simulations, we generally need Fourier transform equation (38) in order to get the time-domain variance $|K_\alpha(\mathbf{r}, t)|^2$ of the random force term distribution.

However, if one were to directly implement Eq. (38), the frequency dependency of the correlator needs to be implemented in terms of a temporal convolution due to the $\Theta(\omega, T)$ term, which is computationally expensive. Instead, the key idea is to use an alternative source $\mathbf{K}'(\mathbf{r}, \omega) = \mathbf{K}(\mathbf{r}, \omega)/\sqrt{\Theta(\omega, T)}$ with a white noise spectrum,

where the correlation is instantaneous in time [47]. Using a random force term with correlation function $\overline{K'_\alpha(\mathbf{r}',\omega)K'^*_\alpha(\mathbf{r}'',\omega)}$ in the FDTD method will allow us to simulate a normalized heat flux spectrum $\overline{\mathbf{S}(\omega)}/\Theta(\omega,T)$. The actual heat flux spectrum $\overline{\mathbf{S}(\omega)}$ is then calculated by simply multiplying this normalized heat flux spectrum by the known function $\Theta(\omega,T)$.

The discretized correlation function of $\mathbf{K}'(\mathbf{r},\omega)$ is

$$\overline{K'_\alpha(\mathbf{r},\omega)K'^*_\beta(\mathbf{r}',\omega')} = \frac{4\sigma\gamma}{\pi\Delta V}\delta_{\alpha\beta}\delta_{\omega\omega'}\delta_{\mathbf{rr}'}. \tag{39}$$

Eq. (39) can be trivially Fourier transformed into the time-domain:

$$\overline{K'_\alpha(\mathbf{r},t)K'^*_\beta(\mathbf{r}',t')} = \frac{4\sigma\gamma}{\pi N\Delta V}\delta_{\alpha\beta}\delta_{tt'}\delta_{\mathbf{rr}'} \tag{40}$$

where N is the number of time steps used in the Fourier transform. Hence, by performing at each time step a random drawing of $\mathbf{K}'$ from a distribution with variance $|K'_\alpha(\mathbf{r},t)|^2$, we can simulate a normalized thermal emission with normalized heat flux spectrum $\overline{\mathbf{S}(\omega)}/\Theta(\omega,T)$. Since the specification of the variance $|K'_\alpha(\mathbf{r},t)|^2$ is the only constraint on the distribution of $\mathbf{K}'$, we can choose a uniform distribution with a range $\pm(12\sigma\gamma/\pi N\Delta V)^{1/2}$.

Finally, we note that although in this section we used a permittivity that is modeled by a single-pole Lorentz function, the method discussed can be implemented with material permittivity that has multiple poles.

5. Comparison of computational approaches

In order to provide a concrete basis for comparison of the computational aspects of the three methods (partial wave scattering, BEM and FDTD), we choose a simple test case: coupled dielectric spheres. In our example, both spheres have a radius $a=800$ nm, are separated by a vacuum gap $d=200$ nm, and the dielectrics are n-doped silicon with a carrier concentration $n=10^{20}$ cm^{-3}, modeled using [50]. The dielectric functions are shown in Fig. 2a. The small sphere size is chosen in part so that all methods can converge in a reasonable time.

All these numerical methods require some discretization or truncation of the problem which introduces error. In the case of BEM, the basis we use in our implementations is the well known RWG (Rao–Wilton–Glisson) functions [51,41], which are defined on a triangulated mesh of the object boundaries. For the FDTD method we use a non-uniform 3D Cartesian grid. In both methods, the intended geometry is only approximated in the spatial discretization procedure. At a more fundamental level, the relevant length scales in the problem must be resolved by incorporating a sufficient number of unknowns in the computation, so we can characterize the behavior of these methods in terms of the scaling behavior of time and memory costs as we vary a and d. As the bodies grow, more unknowns will be required to account for the additional degrees of freedom in the fields. Also, as the bodies are brought closer together, more unknowns are required to resolve the field variations due to near-field interactions. In the following, we will characterize the complexity of the system in terms of the single dimensionless parameter, $\zeta=\max\{k_0a, a/d\}$ [52].

Table 1
A comparison of some computational aspects of three methods for calculating heat transfer between coupled spheres.

Method	Error	Total runtime	Total memory	Time complexity	Space complexity
Partial-wave	0	3 s	<1 Mb	$O(\zeta^4)$	$O(\zeta^2)$
BEM	0.3%	100 h	1.8 Gb	$O(\zeta^6)$	$O(\zeta^4)$
FDTD	14%	4000 h	200 Mb	$O(\zeta^4)$	$O(\zeta^3)$

The numerical results of the three methods, BEM, scattering and FDTD, are shown in Fig. 2b. A summary of the computational performance of the three methods is shown in Table 1. All of our calculations were performed on the SDSC Trestles linux cluster [53].

The scattering method acts as a benchmark of the coupled-sphere problem. There is no discretization error, and the system is small enough that numerical convergence to within 1×10^{-8} can be achieved with fewer than 100 unknowns. The complexity of the scattering method is favorable as well, for highly symmetric geometries. In a system with azimuthal symmetry, each $m=0\ldots m_{max}$ gives a separable problem which requires $N=2l_{max}\propto\zeta$ unknowns. The linear solve is $O(N^3)$ time complexity, but in practice, the time spent calculating the N^2 matrix elements far exceeds the time for the linear solve, provided $N\lesssim10^4$. In general, $m_{max}\propto\zeta$, as well, so for azimuthal symmetric problems, the total time complexity is $O(\zeta^3)$ in practice. In the $\zeta\to\infty$ limit, though, the linear solve eventually dominates so the time complexity is $O(\zeta^4)$. Space complexity is $O(\zeta^2)$, and is not at all prohibitive.

The number of unknowns (edges) in the BEM scales with the area which needs to be resolved, i.e. as $O(\zeta^2)$, so often the limiting computational resource is memory. For our small test case, we used 7000 unknowns, which requires ≈2 Gb to store all the relevant matrices. This is an intentional test to approach maximum problem size we can easily carry out in a 32-bit memory address space. We do not need this many elements to achieve good accuracy. This computation is roughly equally divided between computing BEM matrix elements, and performing matrix operations. For larger systems, matrix operations will dominate the time complexity. The BEM approach gives nearly identical numerical results, whether using direct volume integration or the closed form boundary trace formula, but the latter is more time efficient for larger systems, and there is no ambiguity in how to choose the sources $\mathbf{J}^i$ in the volume integration.

The FDTD method is of a statistical nature; the data shown is an average taken over 40 independent runs, each of which takes ≈100 h to complete. Even after 40 runs, the numerical results have not converged, but the results are consistent with the other methods. Despite these shortcomings, the FDTD method is a valuable tool due to the simplicity of treating arbitrary geometries and inhomogenous dielectrics.

At least two things are worth reemphasizing. First, FDTD is at volumetric method, it actually requires less

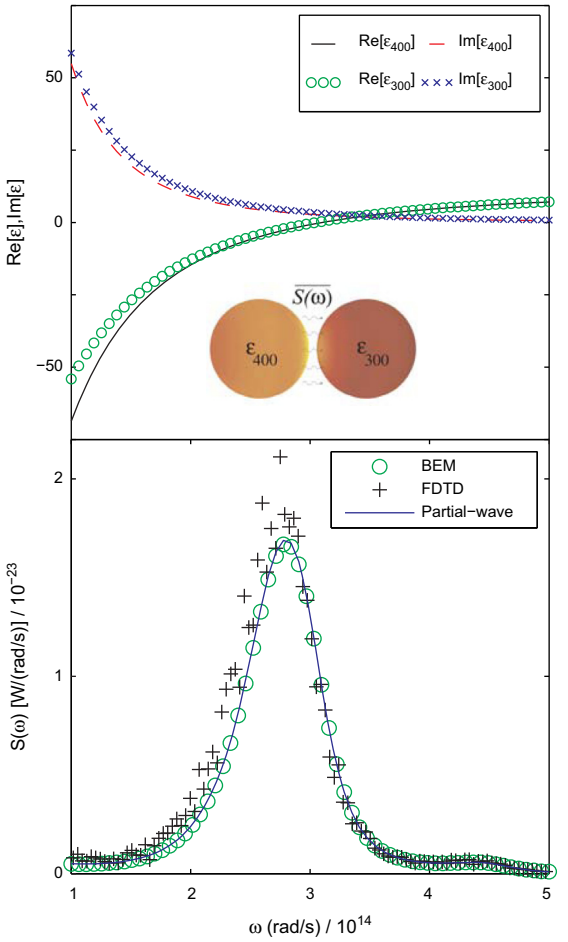

Fig. 2. (a) The dielectric function of hot 400 K and cold 300 K 10^{20} cm^{-3} n-doped Si spheres of radius 800 nm, separated by a 200 nm vacuum gap. The inset graphic is an artistic rendering of theoretical electric field intensity at a hot and cold sphere. (b) Spectral heat transfer $\overline{S(\omega)}$ calculated using three different computational methods.

memory because the system is sparse, whereas our BEM approach results in a dense matrix. Second, BEM also has poor worst case scaling in time complexity, but performs relatively well in a realistically sized system, and there are optimizations which can improve this to $\zeta^4 \log N$ using the pre-corrected FFT algorithm [54,55], or better if adaptive meshes or hierarchical matrices are also used [56].

6. Conclusion

Precision probes of near-field heat transfer have largely focused on plate–plate [3] or sphere–plate [1,2,5] geometries. However, there are important structures which cannot be treated efficiently with the methods described here. For example, one of the most exciting possible applications of near-field heat transfer is near-field thermo-photo-voltaics. The design of effective near-field emitters and absorbers requires tuning the spectral heat transfer between nano-structured surfaces. There has been some work towards this end in 1D grating geometries, using the plane-wave scattering approach [57,58] and the FDTD [49] methods. For more general periodic systems, periodic extensions of the BEM [59] may prove to be an efficient alternative. There is evidence that for nano-scale systems, non-local dielectric effects may come into play [7]. If these non-local effects can be modeled computationally in arbitrary geometries, then light may be shed on near-field heat transfer experiments and the properties of nano-scale dielectrics in general. Certain non-local models [60] can be implemented by modifying the homogenous space Green's function. Since the BEM matrices are constructed from homogenous space Green's functions, BEM methods could perhaps be developed to deal with arbitrary non-local dielectrics.

Acknowledgment

This work is supported by an AFOSR-MURI program (Grant no. FA9550-08-1-0407) and by the Division of Materials Sciences and Engineering, Office of Basic Energy Sciences, the U.S. Department of Energy.

Appendix A. Electromagnetic operator notation

We employ the operator algebra in this paper to make the notation compact. Here we provide a brief discussion of this notation. As an example, in the dyad-vector notation, the electric field $\mathbf{E}(\mathbf{r})$ relates the current density $\mathbf{J}(\mathbf{r})$ through a dyadic Green function,

$$\mathbf{E}_i(\mathbf{r}) = \int d\mathbf{r}' \sum_j \mathbf{G}_{ij}\mathbf{J}_j(\mathbf{r}') \tag{A.1}$$

This formula describes a linear map between $\mathbf{J}(\mathbf{r})$ and $\mathbf{E}(\mathbf{r}')$. In operator language we write this as

$$|\mathbf{E}\rangle = \mathbb{G}_{EE}|\mathbf{J}\rangle \tag{A.2}$$

From any two states $\phi_i(r)$ and $\psi_j(r')$, we can define an operator

$$\mathbb{O}_{ij}(\mathbf{r},\mathbf{r}') \equiv \boldsymbol{\phi}_i^*(\mathbf{r}) \otimes \boldsymbol{\psi}_j(\mathbf{r}') \tag{A.3}$$

We can write this in the operator notation as

$$\mathbb{O} \equiv |\boldsymbol{\phi}\rangle\langle\boldsymbol{\psi}| \tag{A.4}$$

Finally, the trace is defined

$$\mathrm{Tr}\ \mathbb{O} \equiv \sum_i \int d\mathbf{r}\ \mathbb{O}_{ii}(\mathbf{r},\mathbf{r}) \tag{A.5}$$

where integration occurs over all space.

References

[1] Narayanaswamy A, Shen S, Chen G. Near-field radiative heat transfer between a sphere and a substrate. Phys Rev B 2008;78:115303-4.
[2] Rousseau E, Siria A, Jourdan G, Volz S, Comin F, Chevrier J, et al. Radiative heat transfer at the nanoscale. Nat Photonics 2009;3:514–7.
[3] Ottens RS, Quetschke V, Wise S, Alemi AA, Lundock R, Mueller G, et al. Near-field radiative heat transfer between macroscopic planar surfaces. Phys Rev Lett 2011;107:014301-4.
[4] Narayanaswamy A, Gu N. Heat transfer from freely suspended bimaterial microcantilevers. J Heat Transf 2011;133:042501-6.
[5] Guha B, Otey C, Poitras CB, Fan S, Lipson M. Near-field radiative cooling of nanostructures. Nano Lett 2012;12:4546–50.

[6] De Wilde Y, Formanek F, Carminati R, Gralak B, Lemoine PA, Joulain K, et al. Thermal radiation scanning tunnelling microscopy. Nature 2006;444:740–3.
[7] Kittel A, Müller-Hirsch W, Parisi J, Biehs SA, Reddig D, Holthaus M. Near-field heat transfer in a scanning thermal microscope. Phys Rev Lett 2005;95:224301-4.
[8] Otey CR, Lau WT, Fan S. Thermal rectification through vacuum. Phys Rev Lett 2010;104:154301-4.
[9] Basu S, Francoeur M. Near-field radiative transfer based thermal rectification using doped silicon. Appl Phys Lett 2011;98:113106-3.
[10] Zhu L, Otey CR, Fan S. Negative differential thermal conductance through vacuum. Appl Phys Lett 2012;100:044104-3.
[11] Iizuka H, Fan S. Rectification of evanescent heat transfer between dielectric-coated and uncoated silicon carbide plates. J Appl Phys 2012;112:024304-7.
[12] Basu S, Zhang ZM, Fu CJ. Review of near-field thermal radiation and its application to energy conversion. Int J Energy Res 2009;33:1203–32.
[13] Whale MD, Cravalho EG. Modeling and performance of microscale thermophotovoltaic energy conversion devices. IEEE Trans Energy Conv 2002;17:130–42.
[14] Narayanaswamy A, Chen G. Surface modes for near field thermophotovoltaics. Appl Phys Lett 2003;82:3544–6.
[15] Ilic O, Jablan M, Joannopoulos JD, Celanovic I, Soljačić M. Overcoming the black body limit in plasmonic and graphene near-field thermophotovoltaic systems. Opt Exp 2012;20:366–84.
[16] Messina R, Ben-Abdallah P. Graphene-based photovoltaic cells for near-field thermal energy conversion arXiv:1207.1476, 2012.
[17] Rytov SM, Kravtsov YA, Tatarskii VI. Principles of statistical radiophysics. Berlin: Springer-Verlag; 1989.
[18] Janowicz M, Reddig D, Holthaus M. Quantum approach to electromagnetic energy transfer between two dielectric bodies. Phys Rev A 2003;68:043823-17.
[19] Chapuis PO, Volz S, Henkel S, Joulain K, Greffet JJ. Effects of spatial dispersion in near-field radiative heat transfer between two parallel metallic surfaces. Phys Rev B 2008;77:035431-9.
[20] Sellan DP, Landry ES, Sasihithlu K, Narayanaswamy A, McGaughey AJH, Amon CH. Phonon transport across a vacuum gap. Phys Rev B 2012;85:024118-6.
[21] Haus HA. Electromagnetic noise and quantum optical measurements. Berlin: Springer; 2000.
[22] Agarwal GS. Quantum electrodynamics in the presence of dielectrics and conductors. I. Electromagnetic-field response functions and black-body fluctuations in finite geometries. Phys Rev A 1975;11:230–42.
[23] Calzetta E, Hu BL. Stochastic dynamics of correlations in quantum field theory: from the Schwinger–Dyson to Boltzmann–Langevin equation. Phys Rev D 1999;61:025012.
[24] Krüger M, Bimonte G, Emig T, Kardar M. Trace formulae for nonequilibrium Casimir interactions, heat radiation and heat transfer for arbitrary objects. Phys Rev B 2012;86:115423.
[25] Polder D, Van Hove M. Theory of radiative heat transfer between closely spaced bodies. Phys Rev B 1971;4:3303–14.
[26] Loomis JJ, Maris HJ. Theory of heat transfer by evanescent electromagnetic waves. Phys Rev B 1994;50:18517–24.
[27] Biehs SA, Greffet JJ. Influence of roughness on near-field heat transfer between two plates. Phys Rev B 2010;82:245410-8.
[28] Biehs SA, Ben-Abdallah P, Rosa FSS, Joulain K, Greffet JJ. Nanoscale heat flux between nanoporous materials. Opt Exp 2011;19:1088–103.
[29] Pendry JB. Radiative exchange of heat between nanostructures. J Phys: Condens Matter 1999;11:6621–33.
[30] Volokitin AI, Persson BNJ. Radiative heat transfer between nanostructures. Phys Rev B 2001;63:205404-11.
[31] Mulet JP, Joulain K, Carminati R, Greffet JJ. Nanoscale radiative heat transfer between a small particle and a plane surface. Appl Phys Lett 2001;78:2931–3.
[32] Sasihithlu K, Narayanaswamy A. Proximity effects in radiative heat transfer. Phys Rev B 2011;83:161406-4.
[33] Narayanaswamy A, Chen G. Thermal near-field radiative transfer between two spheres. Phys Rev B 2008;77:075125-12.
[34] Krüger M, Emig T, Kardar M. Nonequilibrium electromagnetic fluctuations: heat transfer and interactions. Phys Rev Lett 2011;106:210404-4.
[35] Rahi SJ, Emit T, Graham N, Jaffe RL, Kardar M. Scattering theory approach to electrodynamic Casimir forces. Phys Rev D 2009;80:085021.
[36] John D, Joannopoulos JD, Johnson SG, Winn JN, Meade RD. Photonic crystals: molding the flow of light. Princeton: Princeton University Press; 2008.
[37] McCauley AP, Reid MTH, Krüger M, Johnson SG. Modeling near-field radiative heat transfer from sharp objects using a general 3d numerical scattering technique. Phys Rev B 2012;85:165104-4.
[38] Otey C, Fan S. Numerically exact calculation of electromagnetic heat transfer between a dielectric sphere and plate. Phys Rev B 2011;84:245431-7.
[39] Golyk VA, Krüger M, Kardar M. Heat radiation from long cylindrical objects. Phys Rev E 2012;85:046603-15.
[40] Messina R, Antezza M. Scattering-matrix approach to Casimir–Lifshitz force and heat transfer out of thermal equilibrium between arbitrary bodies. Phys Rev A 2011;84:042102-22.
[41] Hänninen I, Taskinen M, Sarvas J. Singularity subtraction integral formulae for surface integral equations with RWG, rooftop and hybrid basis functions. Prog Electromagn Res 2006;63:243–78.
[42] Reid MTH, Rodriguez AW, White J, Johnson SG. Efficient computation of Casimir interactions between arbitrary 3D objects. Phys Rev Lett 2009;103:040401-4.
[43] Reid MTH, White JK, Johnson SG. Computation of Casimir interactions between arbitrary three-dimensional objects with arbitrary material properties. Phys Rev A 2011;84:010503-4.
[44] Rodriguez AW, Reid MTH, Johnson SG. Fluctuating surface-current formulation of radiative heat transfer for arbitrary geometries. Phys Rev B 2012;86:220302-6.
[45] Chew WC. Waves and fields in inhomogenous media. Berlin: Van Nostrand Reinhold; 1990.
[46] Taflove A, Hagness SC. Computational electrodynamics: the finite-difference time-domain method. 3rd edBoston: Artech House; 2005.
[47] Luo C, Narayanaswamy A, Chen G, Joannopoulos J. Thermal radiation from photonic crystals: a direct calculation. Phys Rev Lett 2004;93:19–22.
[48] Chan D, Soljačić M, Joannopoulos J. Thermal emission and design in one-dimensional periodic metallic photonic crystal slabs. Phys Rev E 2006;74:1–9.
[49] Rodriguez AW, Ilic O, Bermel P, Celanovic I, Joannopoulos JD, Soljačić M, et al. Frequency-selective near-field radiative heat transfer between photonic crystal slabs: a computational approach for arbitrary geometries and materials. Phys Rev Lett 2011;107:114302-5.
[50] Basu S, Lee BJ, Zhang ZM. Infrared radiative properties of heavily doped silicon at room temperature. J Heat Transf 2010;132:023301-8.
[51] Rao SM, Wilton DR, Glisson AW. Electromagnetic scattering by surfaces of arbitrary shape. IEEE Trans Ant Prop 1982;30(3):1982409.
[52] Sasihithlu K, Narayanaswamy A. Convergence of vector spherical wave expansion method applied to near-field radiative transfer. Opt Exp 2011;19(S4):A772–85.
[53] Trestles is an XSEDE San Diego Supercomputer Center cluster consisting of 324 compute nodes, each with 4×2.4 GHz AMD Magny-Cours processors and 64 GB memory capacity. We use 64-bit floating point calculations throughout our examples ⟨http://www.sdsc.edu/us/resources/trestles/⟩.
[54] Reid MTH, Fluctuating surface currents: a new algorithm for efficient prediction of Casimir interactions among arbitrary materials in arbitrary geometries. PhD thesis. MIT; 2011.
[55] Yuan N, Yeo TS, Nie XC, Li LW, Gan YB. Analysis of scattering from composite conducting and dielectric targets using the precorrected-FFT algorithm. J Electromagn Waves Appl 2003;17:499–515.
[56] Bebendorf M, Rjasanow S. Adaptive low-rank approximation of collocation matrices. Computing 2003;70:1–24.
[57] Bimonte G. Scattering approach to Casimir forces and radiative heat transfer for nanostructured surfaces out of thermal equilibrium. Phys Rev A 2009;80:042102-7.
[58] Lussange J, Guérout R, Rosa FSS, Greffet JJ, Lambrecht A, Reynaud S. Radiative heat transfer between two dielectric nanogratings in the scattering approach. Phys Rev B 2012;86:085432-5.
[59] Lee SC, Rawat V, Lee JF. A hybrid finite/boundary element method for periodic structures on non-periodic meshes using an interior penalty formulation for Maxwell's equations. J Comput Phys 2010;229:4934–51.
[60] Garcia de Abajo FJ. Nonlocal effects in the plasmons of strongly interacting nanoparticles, dimers and waveguides. J Phys Chem C 2008;112:17983–7.